Journal of Physics G: Nuclear and Particle Physics

PAPER

Effect of thousands of inelastic couplings on the elastic scattering channel

To cite this article: L C Chamon *et al* 2020 *J. Phys. G: Nucl. Part. Phys.* **47** 105103

View the article online for updates and enhancements.

You may also like

- Corrigendum: Radiative ^{10}Be(n,)^{11}Be capture at thermal and astrophysical energies (2016 *J. Phys. G: Nucl. Part. Phys.* **43** 095201)
S B Dubovichenko and A V Dzhazairov-Kakhramanov
- Discovery of ASKAP J173608.2–321635 as a Highly Polarized Transient Point Source with the Australian SKA Pathfinder
Ziteng Wang, David L. Kaplan, Tara Murphy et al.
- A Large Catalog of Accurate Distances to Local Molecular Clouds: The *Gaia* DR2 Edition
Catherine Zucker, Joshua S. Speagle, Edward F. Schlafly et al.

Recent citations

- São Paulo potential version 2 (SPP2) and Brazilian nuclear potential (BNP)
L.C. Chamon *et al*
- Understanding the mechanisms of nuclear collisions: A complete study of the B10+Sn120 reaction
L. R. Gasques *et al*

This content was downloaded from IP address 143.107.128.45 on 12/01/2022 at 19:06

IOP Publishing Journal of Physics G: Nuclear and Particle Physics
J. Phys. G: Nucl. Part. Phys. **47** (2020) 105103 (23pp) https://doi.org/10.1088/1361-6471/aba424

Effect of thousands of inelastic couplings on the elastic scattering channel

L C Chamon, L R Gasques and J C Zamora

Universidade de Sao Paulo, Instituto de Fisica, Rua do Matao, 1371, 05508-090, Sao Paulo, SP, Brazil

E-mail: lchamon@if.usp.br

Received 20 May 2020, revised 30 June 2020
Accepted for publication 8 July 2020
Published 28 August 2020

Abstract

We describe a new method to solve coupled equations, that arises from the coupled-channel formalism applied to nuclear reactions involving the elastic and inelastic scattering processes. The new technique is faster and presents better numerical convergence than other usual methods. To illustrate the method, in the present paper we have analyzed data for the ^{4}He + ^{208}Pb system at $E_{\text{lab.}} = 120$ and 139 MeV, including thousands of inelastic states with excitation energies up to 80 MeV. However, as a limitation, the method can be used only in the case of couplings connecting directly the inelastic channels to the elastic one, without couplings among the inelastic states.

Keywords: nuclear reactions, coupled-channel formalism, elastic scattering

(Some figures may appear in colour only in the online journal)

1. Introduction

Many different processes are usually present in nuclear reactions involving heavy nuclei, such as: elastic scattering, Coulomb and nuclear excitation of inelastic states, transfer of nucleons and clusters, fusion, break-up, etc. This complicated problem is many times approached in the context of the coupled-channel (CC) formalism (see e.g. references [1, 2]). In this case, generally the elastic scattering with a few peripheral reaction channels are explicitly included in coupled equations (CE), while the absorption of flux due to the other channels, mainly fusion, is simulated through an imaginary part included in the optical potential.

Some numerical method must be assumed to solve the CE. Three of the methods frequently used are briefly presented in appendix A. Numerical problems can occur in some cases, and the convergence of the solution can not be reached depending on the number of coupled states involved in the calculations and on the characteristics of these couplings. Some computational codes have thus been developed to perform CC calculations through different methods (see e.g

ECIS [3, 4], FRESCO [5] and *R*-matrix package [6] codes). Even so, difficulties to obtain the numerical convergence of the solution of the CE can still be found in several cases even using these powerful codes. In addition, the inclusion of many states in the calculations, increasing thus the number of CE, can make the time of computation prohibitive.

The elastic scattering process has been studied for many systems in a very wide energy range. Optical model (OM) analyses assuming a single-channel Schrödinger equation, have been largely employed to fit the experimental cross sections, with determination of the respective optical potentials (OP) that describe the data. An important energy-dependence of these phenomenological OP has been reported [7]. Based on this fact, several theoretical models have been proposed to explain this energy-dependence, which has been associated to the effective nucleon–nucleon interaction (see e.g. references [8–10]). However, in a recent paper [11] we studied the effect on the elastic scattering process of couplings to inelastic states at high excitation energies. As an example, we have chosen the case of ^{4}He + ^{208}Pb in near-barrier and intermediate energies. We demonstrated that a significant part of the energy-dependence of the phenomenological OP could be in fact related to these inelastic couplings. Nevertheless, there is a huge amount of ^{208}Pb excited states that might be contributing to this effect, with excitation energies that can reach many tens of MeV. In reference [11], we did not have a computational code to perform this type of CC calculations and, thus, we simulated the effect of a large number of states through the coupling of only six states (with large values for the deformation parameters). With the purpose of improving the calculations, we have found a new method capable to solve CE involving a very large number of inelastic states with quite high excitation energies.

In this paper, we present a computationally efficient method to solve CE suitable for large-scale CC calculations. The new method is faster and presents a lesser degree of problems with numerical convergence than the usual ones. However, the method has an important limitation: it is appropriate to treat couplings only in first order, in which the inelastic states are directly coupled to the elastic channel (there is no coupling among the inelastic states). As an example of application of the method, we analyze elastic and inelastic scattering data for ^{4}He + ^{208}Pb at $E_{\rm lab.} = 120$ and 139 MeV. We also present tests simulating couplings that involve more than ten thousand CE, to states of high excitation energies that reach up to 80 MeV.

2. The new method

Let us consider the following set of $M + 1$ CE:

$$\hat{H}_J\, f_0(r) + \sum_{i=1}^{M} V_i(r)\, f_i(r) = E\, f_0(r), \tag{1}$$

$$\hat{H}_{L_i}\, f_i(r) + V_i^*(r)\, f_0(r) = (E - E_i^*)\, f_i(r), \tag{2}$$

where

$$\hat{H}_L = -\frac{\hbar^2}{2\mu}\frac{\mathrm{d}^2}{\mathrm{d}r^2} + \frac{L(L+1)\hbar^2}{2\mu r^2} + V_{\rm C}(r) + V_{\rm N}(r) + iW(r). \tag{3}$$

We adopt the sub-index $i = 0$ in equation (1) for the elastic channel, and $i = 1$ to M for the inelastic states according to (2). It is implied that the orbital angular momentum L depends on the state i through the L_i symbol. Let us restrict ourselves to the case where all inelastic channels are open, i.e. with excitation energies $E_i^* < E$.

The wave-functions must obey the following boundary conditions:

$$f_0(r \to 0) = b_0\, r^{J+1}; \qquad f_i(r \to 0) = b_i\, r^{L_i+1}, \tag{4}$$

$$f_0(r \to \infty) = \frac{i}{2}\left(H_0^- - S_0\, H_0^+\right), \tag{5}$$

$$f_i(r \to \infty) = -\frac{i}{2} S_i\, H_i^+, \tag{6}$$

where

$$H_i^{\pm}(r) = G_i(r) \pm F_i(r). \tag{7}$$

G and F are the Coulomb functions (which depend on $E - E_i^*$ and L_i), and b_i are complex constants. The present method can be generalized to closed channels, involving then the Whitaker functions in the boundary conditions instead of the Coulomb ones. Since the inelastic couplings, $V_i^*(r)$ in equation (2), are assumed as the complex conjugate of the elastic couplings, $V_i(r)$ in equation (1), the flux conservation is guaranteed (as defined ahead).

The CC problem is reduced to obtain the solutions of the CE, i.e.: the respective wave-functions $f_i(r)$ and corresponding S matrix. Usually, this problem is solved considering a certain matching radius $R_{\max}$, in which the effects of the couplings and of the nuclear force are negligible. We also adopt this procedure here, assuming that equations (5) and (6) are valid for $r \approx R_{\max}$. As previously mentioned, we present a brief review of three methods often used to solve CE in appendix A.

2.1. Optical and irregular functions

We define the optical function, $f^{\rm op}(r)$, as the solution of the following single-channel Schrödinger equation and boundary conditions:

$$\hat{H}_{L_i}\, f_i^{\rm op}(r) = (E - E_i^*)\, f_i^{\rm op}(r), \tag{8}$$

$$f_i^{\rm op}(r \approx R_{\max}) = \frac{i}{2}\left(H_i^- - S_i^{\rm op}\, H_i^+\right), \tag{9}$$

$$f_i^{\rm op}(r \to 0) = c_i\, r^{L_i+1}. \tag{10}$$

The irregular function, $f^{\rm irr}(r)$, also obeys (8), but now with the following boundary condition:

$$f_i^{\rm irr}(r \approx R_{\max}) = H_i^+. \tag{11}$$

Equation (8) is uncoupled and, therefore, it can easily be integrated using the Cowell's method [12, 13]. In the case of the optical function, the integration is performed from $r = 0$ to $R_{\max}$, using equation (10), while for the irregular function the integration starts at $R_{\max}$, through equation (11), and is performed towards the inner region.

2.2. The Green equations

We define:

$$k_i = \frac{1}{\hbar}\sqrt{2\mu\left(E - E_i^*\right)}. \tag{12}$$

Through the Green method, we have the following pseudo-solutions (see e.g. reference [4]):

$$f_0(r) = f_0^{\rm op}(r) - \frac{k_0}{E}\left\{ f_0^{\rm op}(r)\int_r^\infty f_0^{\rm irr}(r')\sum_{i=1}^{M}\left[V_i(r')\,f_i(r')\right]\mathrm{d}r' + f_0^{\rm irr}(r)\int_0^r f_0^{\rm op}(r')\sum_{i=1}^{M}\left[V_i(r')\,f_i(r')\right]\mathrm{d}r'\right\}, \tag{13}$$

$$f_i(r) = -\frac{k_0^2}{k_i E}\left[f_i^{\rm op}(r)\int_r^\infty f_i^{\rm irr}(r')V_i^*(r')\,f_0(r')\mathrm{d}r' + f_i^{\rm irr}(r)\int_0^r f_i^{\rm op}(r')V_i^*(r')\,f_0(r')\mathrm{d}r'\right]. \tag{14}$$

The S matrix is obtained from:

$$S_0 = S_0^{\rm opt} - 2i\,\frac{k_0}{E}\int_0^\infty f_0^{\rm op}(r')\sum_{i=1}^{M}\left[V_i(r')\,f_i(r')\right]\mathrm{d}r', \tag{15}$$

$$S_i = -2i\,\frac{k_0^2}{k_i E}\int_0^\infty f_i^{\rm op}(r')V_i^*(r')\,f_0(r')\mathrm{d}r'. \tag{16}$$

Actually, equations (13) and (14) are not solutions of the CE since the wave-functions are found on both the left and right sides of the equations.

2.3. Rearranging equations

Inserting (14) in (13), we obtain:

$$f_0(r) = f_0^{\rm op}(r) + f(r), \tag{17}$$

with

$$f(r) = \left(\frac{k_0}{E}\right)^2\left\{ f_0^{\rm op}(r)\int_r^\infty f_0^{\rm irr}(r')\left[I_1(r') + I_2(r')\right]\mathrm{d}r' + f_0^{\rm irr}(r)\int_0^r f_0^{\rm op}(r')\left[I_1(r') + I_2(r')\right]\mathrm{d}r'\right\}, \tag{18}$$

where

$$I_1(r') = \sum_{i=1}^{M}\frac{k_0}{k_i}\,V_i(r')\,f_i^{\rm op}(r')\int_{r'}^\infty f_i^{\rm irr}(r'')V_i^*(r'')\,f_0(r'')\,\mathrm{d}r'', \tag{19}$$

$$I_2(r') = \sum_{i=1}^{M}\frac{k_0}{k_i}\,V_i(r')\,f_i^{\rm irr}(r')\int_0^{r'} f_i^{\rm op}(r'')V_i^*(r'')\,f_0(r'')\,\mathrm{d}r''. \tag{20}$$

Notice that equations (17) to (20) involve only one unknown wave-function, the elastic one $f_0(r)$, since the optical and irregular functions in these equations can easily be obtained (as explained in section 2.1). Thus, if one solves (17) to (20) obtaining $f_0(r)$, the CC problem is solved. In fact, with $f_0(r)$ the inelastic wave-functions can be obtained from (14) and the S matrix can be calculated using (15) and (16).

The method presented here is based on the solution of (17) to (20) that, as already mentioned, have only $f_0(r)$ as unknown wave-function. These equations were obtained inserting (14) in (13), and could be derived just because the right side of equation (14) does not contain any wave-function of inelastic states (it involves only $f_0(r)$). This characteristic is related to equation (2), which does not include any coupling among inelastic states (it only couples the inelastic state to the elastic channel). Therefore, our method is valid only within this condition: no direct coupling among the inelastic states.

Taking into account the boundary conditions (4) and (5), we must have:

$$f(r=0)=0, \tag{21}$$

$$f(r\approx R_{\max})=-\frac{i}{2}S\,H_0^+, \tag{22}$$

where the S matrix element relative to the elastic channel is related to S by:

$$S_0=S_0^{\rm op}+S. \tag{23}$$

Indeed, equation (22) (with $r\approx R_{\max}$) is equivalent to the two following equations (with $r=R_{\max}$):

$$f(r=R_{\max})=-\frac{i}{2}S\,H_0^+, \tag{24}$$

$$f'(r=R_{\max})=-\frac{i}{2}S\,H'^+_0, \tag{25}$$

where f' and H' represent derivatives in relation to r. Combining (24) and (25), we obtain a constraint equation:

$$\left[fH'-Hf'\right]_{r=R\max}=0. \tag{26}$$

If $f(r)$ were known, it would be possible to obtain the wave-function $f_0(r)$ for the elastic channel from (17), and thus solving the CC problem. However, $f(r)$ depends on $f_0(r)$ through equations (18) to (20). Thus, we should rearrange a few more equations to move forward with our method.

In view of (17), (19) and (20) can be rewritten as:

$$I_1(r')=I_1^{\rm op}(r')+T_1(r'), \tag{27}$$

$$I_2(r')=I_2^{\rm op}(r')+T_2(r'), \tag{28}$$

where $I_1^{\rm op}(r')$ and $I_2^{\rm op}(r')$ are still calculated with equations (19) and (20), but now with $f_0^{\rm op}(r)$ in these equations instead of $f_0(r)$. We define:

$$T_1(r')=\sum_{i=1}^{M}\frac{k_0}{k_i}\,V_i(r')\,f_i^{\rm op}(r')\int_{r'}^{\infty}f_i^{\rm irr}(r'')V_i^*(r'')\,f(r'')\,{\rm d}r'', \tag{29}$$

$$T_2(r')=\sum_{i=1}^{M}\frac{k_0}{k_i}\,V_i(r')\,f_i^{\rm irr}(r')\int_{0}^{r'}f_i^{\rm op}(r'')V_i^*(r'')\,f(r'')\,{\rm d}r''. \tag{30}$$

That is, $T_1(r')$ and $T_2(r')$ are also calculated with equations (19) and (20), but this time with $f(r)$ instead of $f_0(r)$. With this, the calculation of $I_1^{\rm op}(r')$ and $I_2^{\rm op}(r')$ can be performed without

knowing $f_0(r)$. Thus, in order to obtain $f(r)$ from equation (18), using (27) and (28), only the $T_1(r')$ and $T_2(r')$ terms are unknown *a priori*, since they are obtained from equations (29) and (30) that involve the $f(r)$ itself.

2.4. The new method

The method proposed here is similar to that used in R-matrix calculations [6], discussed in appendix A. The function $f(r)$ is expanded in the region $0 \leqslant r \leqslant R_{\max}$ in the following form:

$$f(r) \approx \sum_{n=1}^{N} a_n \phi_n(r). \tag{31}$$

Given a certain basis of known $\phi_n(r)$ functions, the solution of the CC problem is obtained with the determination of the set of the N complex constants a_n. Considering the boundary condition (21) and the constraint (26), we must have:

$$\phi_n(r=0) = 0, \tag{32}$$

$$\sum_{n=1}^{N} a_n \left[\phi_n H'^{+}_0 - \phi'_n H^{+}_0\right]_{r=R_{\max}} = 0. \tag{33}$$

Taking (18) and (27)–(31) into account, we obtain the following equation:

$$\sum_{n=1}^{N} a_n \left[\phi_n(r) - g_n(r)\right] \approx h(r), \tag{34}$$

where

$$h(r) = \left(\frac{k_0}{E}\right)^2 \left\{ f_0^{\rm op}(r) \int_r^{\infty} f_0^{\rm irr}(r') \left[I_1^{\rm op}(r') + I_2^{\rm op}(r') \right] \, {\rm d}r' + f_0^{\rm irr}(r) \int_0^{r} f_0^{\rm op}(r') \, \left[I_1^{\rm op}(r') + I_2^{\rm op}(r') \right] \, {\rm d}r' \right\}, \tag{35}$$

$$g_n(r) = \left(\frac{k_0}{E}\right)^2 \left\{ f_0^{\rm op}(r) \int_r^{\infty} f_0^{\rm irr}(r') \left[T_1^{n}(r') + T_2^{n}(r') \right] \, {\rm d}r' + f_0^{\rm irr}(r) \int_0^{r} f_0^{\rm op}(r') \, \left[T_1^{(n)}(r') + T_2^{(n)}(r') \right] \, {\rm d}r' \right\}, \tag{36}$$

$$T_1^{(n)}(r') = \sum_{i=1}^{M} \frac{k_0}{k_i} V_i(r') \, f_i^{\rm op}(r') \int_{r'}^{\infty} f_i^{\rm irr}(r'') V_i^*(r'') \, \phi_n(r'') \, {\rm d}r'', \tag{37}$$

$$T_2^{(n)}(r') = \sum_{i=1}^{M} \frac{k_0}{k_i} V_i(r') \, f_i^{\rm irr}(r') \int_{0}^{r'} f_i^{\rm op}(r'') V_i^*(r'') \, \phi_n(r'') \, {\rm d}r''. \tag{38}$$

Different from $T_1(r')$ and $T_2(r')$, $T_1^{(n)}(r')$ and $T_2^{(n)}(r')$ can be obtained even without knowing $f(r)$, since they are related through (37) and (38) to the basis $\phi_n(r)$ adopted in the calculations.

Observe that all terms involved in equation (34) are known (calculable) except the a_n coefficients. Thus, we solve the CC problem by obtaining the set of a_n values that is an approximate

solution of equation (34) in the region $0 \leqslant r \leqslant R_{\max}$, considering the constraints (32) and (33). With the a_n values, one obtains $f(r)$ with (31), S with (24) and S_0 with (23).

2.5. The basis

We must choose an appropriate basis of $\phi_n(r)$ functions to be used in expansion (31), with the constraint (32). In this paper, we assume the Lagrange functions (see e.g. [6]):

$$\phi_n(r) = (-1)^{K+n} \frac{r}{R_{\max}\, x_n} \sqrt{R_{\max}\, x_n(1-x_n)}\, \frac{P_K(2r/R_{\max}-1)}{r - R_{\max}\, x_n}, \tag{39}$$

where $P_K(x)$ is the Legendre polynomial of degree K and x_n are the solutions of the equation:

$$P_K(2x_n - 1) = 0. \tag{40}$$

There are K x_n values in the region of interest (between 0 and 1). It follows some properties of the Lagrange functions that we use in our calculations.

We define the ϵ_n values by:

$$\epsilon_n = 2x_n - 1, \tag{41}$$

and thus $P_K(\epsilon_n) = 0$. The weights W_n are given by:

$$W_n = \frac{2}{(1-\epsilon_n^2)\left[\frac{\mathrm{d}P_K}{\mathrm{d}x}(\epsilon_n)\right]^2}. \tag{42}$$

It is possible to show that:

$$\phi_n(x_m\, R_{\max}) = \frac{1}{\sqrt{W_n}}\, \delta_{nm}, \tag{43}$$

$$\phi_n(R_{\max}) = (-1)^{K+n} \frac{1}{\sqrt{R_{\max}\, x_n(1-x_n)}}, \tag{44}$$

$$\frac{\mathrm{d}\phi_n}{\mathrm{d}r}(R_{\max}) = (-1)^{K+n} \frac{[K(K+1)(R_{\max}-r_n) - r_n]\, \sqrt{r_n(1-x_n)}}{r_n(R_{\max}-r_n)^2}, \tag{45}$$

where $r_n = x_n R_{\max}$.

2.6. Numerical calculations

Let us consider a Legendre polynomial of degree K. With this, the number of ϕ_n functions (and a_n parameters) is $N = K$. However, the constraint (33) reduces the number of free parameters to $N_{\mathrm{p}} = N - 1$.

We choose a set of discrete r_j values, with $j = 1, 2, \ldots, N_r$, in the region $0 \leqslant r \leqslant R_{\mathrm{Max}}$. Applying equation (34) to these r_j values, we obtain a set of $j = 1$ to N_r equations for the (x_{jn}, y_j) values, with unknown a_n parameters, given by:

$$\sum_{n=1}^{N} x_{jn}\, a_n \approx y_j, \tag{46}$$

where

$$x_{jn} = \phi_n(r_j) - g_n(r_j), \tag{47}$$

$$y_j = h(r_j). \tag{48}$$

The parameters are constrained by:

$$\sum_{n=1}^{N} a_n v_n = 0, \tag{49}$$

$$v_n = \left[\phi_n H'^{+}_0 - \phi'_n H^{+}_0\right]_{r=R_{\max}}. \tag{50}$$

Note that equations (46) and (49) are equivalent to (34) and (33), respectively. Thus, the x_{jn}, y_j and v_n values are known, and we need to obtain the values of the coefficients a_n. The (x_{jn}, y_j) values can be named as the set of 'experimental' points, that should be fitted as well as possible through equation (46), considering a finite number of adjustable a_n parameters.

The solution of equation (46) with the constraint (49) can be obtained by using the following matrices:

$$A = \begin{pmatrix} a_1 \\ a_2 \\ \vdots \\ a_N \end{pmatrix} \tag{51}$$

$$Y = \begin{pmatrix} y_1 \\ y_2 \\ \vdots \\ y_{N_r} \end{pmatrix} \tag{52}$$

$$G = \begin{pmatrix} v_1 v_2 \dots v_N \end{pmatrix} \tag{53}$$

$$X = \begin{pmatrix} x_{11} & x_{12} & \dots & x_{1N} \\ x_{21} & x_{22} & \dots & x_{2N} \\ \vdots & \vdots & \vdots & \vdots \\ x_{N_r,1} & x_{N_r,2} & \dots & x_{N_rN} \end{pmatrix} \tag{54}$$

With this, we must solve the matricial equation given by:

$$X \times A = Y. \tag{55}$$

With this purpose, first we obtain the auxiliary matrices:

$$H = X^{\dagger} \times X, \tag{56}$$

$$B = H^{-1} \times G^{\dagger}, \tag{57}$$

$$C = -G \times B, \tag{58}$$

$$V_A = H^{-1} + B \times C^{-1} \times B^{\dagger}, \tag{59}$$

and the solution for the parameters is then obtained from [14]:

$$A = V_A \times X^{\dagger} \times Y. \tag{60}$$

V_A is the covariance matrix of the adjusted parameters. Thus, the CC problem is solved.

For the set of the r_j values, we have assumed $r_j = j \times \Delta r$, $j = 1, 2, \ldots, N_r$, with $\Delta r = R_{\max}/N_r$. Typically, we have used $\Delta r = 0.02$ fm. The degree K of the Legendre polynomial should be varied in order to check the convergence of the results. We have used $60 \leqslant K \leqslant 200$.

After obtaining the solution for the set of a_n parameters, we check the numerical precision resulting for the constraint (49), by comparing the value obtained for $|\sum a_n v_n|$ with the average value of the set of all $|a_n v_n|$ involved in the summation. Normally, we have obtained a precision ($|\sum a_n v_n|/|a_n v_n|$) better than 0.1%.

As a further check of the numerical convergence of the calculations, we verify the balance of flux involved in the reaction. For each total angular momentum J, the partial reaction cross section is given by:

$$\sigma_R^{(J)} = \frac{\pi}{k_0^2}\,(2J+1)\,\left(1 - |S_0|^2\right). \tag{61}$$

Still for each J, the (angle integrated) inelastic cross section for each excited state is obtained from:

$$\sigma_i^{(J)} = \frac{\pi\, k_i}{k_0^3}\,(2J+1)\,|S_i|^2. \tag{62}$$

We calculate the partial J contribution for the fusion process as [15]:

$$\sigma_{\rm F}^{(J)} = -\frac{4\pi}{k_0\, E}\,(2J+1)\sum_{i=0}^{M}\int_0^{\rm Rmax} W(r)\,|f_i(r)|^2\,{\rm d}r. \tag{63}$$

The flux conservation implies that:

$$\sigma_R^{(J)} = \sigma_{\rm F}^{(J)} + \sum_{i=1}^{M}\sigma_i^{(J)}. \tag{64}$$

We test this relation for all J values, and typically we have obtained precision better than 1% (in the comparison between the values obtained for both sides of this equation).

It is important to discuss another characteristic of the calculation. We also test the adherence of the solution as a function of the distance r_j. This adherence is evaluated as follows. With the resulting A matrix, we obtain the 'theoretical' $Y_{\rm teo}$ matrix given by:

$$Y_{\rm teo} = X \times A. \tag{65}$$

Then, we compare the elements of this $Y_{\rm teo}$ matrix with all the 'experimental' $y_{\rm exp}(r_j)$ obtained with (48), through:

$$\Delta y_j = 2 \times \frac{|y_{\rm exp}(r_j) - y_{\rm teo}(r_j)|}{|y_{\rm exp}(r_j)| + |y_{\rm teo}(r_j)|}. \tag{66}$$

Thus, Δy_j represents the relative precision with which each $y(r_j)$ of (48) has been reproduced by the solution obtained from the matricial equation. On the one hand, we have obtained a precision better than 5%, except at the region of internal distances in the case of large J values. This is expected due to the large centrifugal repulsion between the nuclei related to large angular momenta. On the other hand, this deviation at inner distances is, in fact, not much

important, except when it affects the cross sections. As already commented, we always test the flux conservation through (64), which involves the wave-functions in the complete range of distances according to (63).

To finalise this section, we comment that, in many cases, we have successfully checked the results of our CC calculations performed with the new method, through the comparison with those obtained with an usual method to solve CE (the traditional method discussed in appendix A). We provide examples of this in section 4. The new method provides convergent results even in cases where the traditional one fails. In the cases where both methods work, the new method is still useful since its computing time is reduced when dealing with a very large number of coupled states.

3. The coupling model and the polarization potential

We emphasise that the essence of our method was already described in the last section, and it does not depend on further details of the coupling model. In this section, we describe the model that we have assumed to analyze the data in the present work.

We deal with a nuclear reaction in which both target and projectile are even–even nuclei with spin zero. We label with S the (integer) spin of a particular excited state. For each J value, there are at most $S+1$ CE associated to this state, with coupling potentials given by:

$$V_i(r) = \frac{i^{L_i-J}}{\sqrt{4\pi}}\, C^{J\,S\,L_i}_{0\,0\,0}\, \left[-\delta_{\rm N}\,\frac{\partial V_{\rm N}(r)}{\partial r} + \delta_{\rm C}\,\frac{3Z_1Z_2R_{\rm C}^{S-1}}{2S+1}\,V_{\rm C}^{\rm coup}(r)\right], \tag{67}$$

$$V_{\rm C}^{\rm coup}(r) = \begin{cases} \dfrac{1}{r^{S+1}} & \text{for } r \geqslant R_{\rm C} \\ \dfrac{r^S}{R_{\rm C}^{2S+1}} & \text{for } r \leqslant R_{\rm C} \end{cases} \tag{68}$$

where $\delta_{\rm N}$ and $\delta_{\rm C}$ are the respective nuclear and Coulomb deformations for this state. The Clebsch–Gordan coefficients in the coupling potentials guarantee the total angular momentum conservation. For a given J value, the orbital angular momentum for the i coupling is restricted to the region $|J-S| \leqslant L_i \leqslant J+S$, with the condition that $J+L_i+S$ is even. We have not included Coulomb contributions in the couplings for $S=0$, assuming $\delta_{\rm C}=0$ in these cases.

Equation (1) can be rewritten as:

$$\left[-\frac{\hbar^2}{2\mu}\frac{{\rm d}^2}{{\rm d}r^2} + \frac{J(J+1)\hbar^2}{2\mu r^2} + V_{\rm C}(r) + V_{\rm N}(r) + iW(r) + U^{(J)}_{\rm pol}(r;E)\right] f_0^{(J)}(r) = E\, f_0^{(J)}(r), \tag{69}$$

where we defined the trivially local-equivalent polarization (TLEP) potential as

$$U^{(J)}_{\rm pol}(r;E) = \frac{\sum_{i=1}^{M} V_i(r)\, f_i^{(J)}(r)}{f_0^{(J)}(r)}. \tag{70}$$

The super index $^{(J)}$ is now included in the wave-functions just to avoid confusion. Equation (69) has the form of a single-channel Schrödinger equation for the elastic scattering, where the effect of the explicit couplings of (1) where exchanged in (69) by the TLEP. The TLEP is complex and clearly dependent on J and E. In reference [17], it was numerically demonstrated the connection between the energy dependence of the OP with CC effects for ^{16}O + ^{208}Pb at

Coulomb energies. This connection has theoretically been demonstrated within the Feshbach projection formalism. As proposed in [17], we perform an average over J and define the mean-polarization potential (MPP) at a certain energy E as:

$$U_{\rm pol}(r) = V_{\rm pol}(r) + iW_{\rm pol}(r) = \frac{\sum c_j \left| f_0^{(J)}(r) \right|^2 U_{\rm pol}^{(J)}(r;E)}{\sum c_j \left| f_0^{(J)}(r) \right|^2}, \tag{71}$$

$$c_J = (2J+1)\left(1 - \left|S_0^{(J)}\right|^2\right). \tag{72}$$

In the next section, we use the TLEP and the MPP to evaluate the effect of the inelastic couplings on the OP for the elastic channel.

4. Data analyses

From the figures of reference [18], we have obtained experimental angular distributions of elastic scattering and excitation of the first ^{208}Pb 3^- state ($E^* = 2.614$ MeV), for ^{4}He + ^{208}Pb at $E_{\rm lab} = 139$ MeV. We have also obtained data for the same system, but at $E_{\rm lab} = 120$ MeV, from reference [19]. In the latter case, the angular distributions were taken in a significantly smaller angular region, but the data set comprises many excited states of ^{208}Pb up to the giant resonances region. Furthermore, information about the continuum in inelastic scattering (up to 80 MeV excitation energy) was also extracted from the double-differential cross sections reported in reference [19].

The elastic scattering angular distribution at 139 MeV was very well adjusted in reference [18] within the context of the single-channel OM. For the OP, the authors of that reference assumed a Woods-Saxon shape, with the following parameter values: $V_0 = 155$ MeV, $R_0 = 7.596$ fm, $a = 0.677$ fm, $W_0 = 23.26$ MeV, $R_i = 8.757$ fm, $a_i = 0.733$ fm. We adopt the same OP for $V_{\rm N}(r) + iW(r)$ in equations (1) and (2). In figure 1, we show elastic scattering data and theoretical single-channel OM cross sections at $E_{\rm lab} = 120$ and 139 MeV. The OM calculations with this OP provides a good data description in both energies. If the effect of the couplings is small, the theoretical elastic scattering cross sections calculated within OM and CC are expected to be very similar. We will see that this is not true at all.

Given that the OP assumed in our calculations provides a very good description of the elastic scattering data (within the context of the OM—without couplings), we have obtained the deformation parameter values for the inelastic states through the corresponding data fit, making use of the distorted wave Born approximation (DWBA—see appendix A.2). With this procedure, we consider that the values obtained for the deformations are realistic. We have assumed $R_{\rm C} = 6.73$ for the radius involved in the Coulomb coupling of equations (67) and (68). However, we verified that the Coulomb couplings provide negligible contribution to the cross sections and, therefore, the data fit is not sensitive to the $\delta_{\rm C}$ values. Thus, we have assumed $\delta_{\rm C} = \delta_{\rm N}$ for all states with $S > 0$, except for the giant resonances for which we adopted $\delta_{\rm C} = 0$. Table 1 presents the values of the coupling parameters corresponding to the discrete ^{208}Pb states considered in the present work. In figure 2, we illustrate the fit to the data for four states chosen as example, including a wide angular distribution for the first 3^- state (measured at $E_{\rm lab.} = 139$ MeV), and a giant resonance (measured at $E_{\rm lab.} = 120$ MeV) at the excitation energy of $E^* = 13.9$ MeV. Clearly, the theoretical DWBA cross sections are in good agreement with the data.

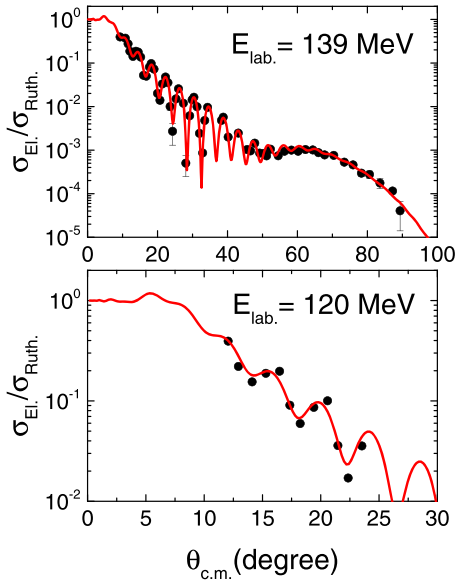

Figure 1. Data and theoretical single-channel OM cross sections for the elastic scattering at two energies for ^{4}He + ^{208}Pb.

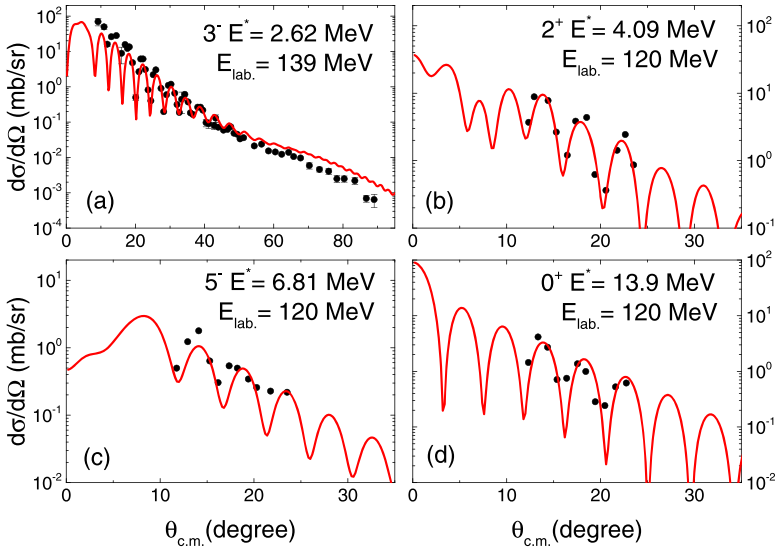

Figure 2. Data and theoretical DWBA cross sections for the inelastic excitation of four ^{208}Pb states.

4.1. The continuum in inelastic scattering

In figures 1 and 2 from reference [19], that present excitation-energy spectra for measurements at $E_{\text{lab.}} = 120$ MeV, one can see several peaks corresponding to the inelastic excitation of discrete states of low excitation energies (those of table 1), and a continuum that comes from

Table 1. Parameter values for some discrete excited states of ^{208}Pb.

State	E^*(MeV)	Spin	δ_N(fm)
1	2.62	3^-	0.90
2	3.20	5^-	0.45
3	3.71	5^-	0.30
4	4.09	2^+	0.51
5	4.32	4^+	0.55
6	4.42	6^+	0.45
7	4.70	3^-	0.28
8	4.83	1^-	0.25
9	4.95	3^-	0.25
10	5.14	2^+	0.17
11	5.35	3^-	0.31
12	5.58	3^-	0.51
13	5.82	4^+	0.36
14	6.20	2^+	0.19
15	6.37	2^+	0.26
16	6.58	2^+	0.15
17	6.81	5^-	0.28
18	7.29	2^+	0.15
19	7.52	2^+	0.26
20	8.34	4^+	0.26
21	10.9	2^+	0.83
22	13.9	0^+	0.51

different reaction mechanisms. The continuum in ^{4}He + ^{208}Pb begins at about $E^* = 10$ MeV and has a wide range that reaches at least up to $E^* = 80$ MeV (it is not possible to see the end, since there is a threshold in the spectra probably due to electronics). The yield of the continuum decreases quite slowly with the increasing of the excitation energy. For instance, the yield at $E^* = 50$ MeV is only about 20% smaller than that at $E^* = 10$ MeV. Thus, in addition to the contribution of the discrete states of table 1, we also want to estimate the effect on the elastic channel of the couplings to the nuclear reactions involved in this continuum. Such nuclear reactions are, of course, not only related to inelastic scattering, but also include many other components like transfer reactions and multistep processes [20]. In fact, we believe that the yield in the region of the continuum might also have a small contribution of instrumental background due to beam halo or multiple scattering in the target. As we intend only an estimate of the effect of the physical continuum on the elastic, we simulate its contribution by considering inelastic couplings to a large number of discrete states with excitation energies up to 80 MeV. In what follows, we explain how we have done these calculations, which were performed mostly at $E_{lab} = 120$ MeV, for which we have experimental information about the continuum plus background (CPB).

First of all, we studied what is the density of discrete states that simulates with appropriated precision an uniform continuum. We adopted a bin of excitation energy in the region: $10 \leqslant E^* \leqslant 20$ MeV, and performed calculations considering different spins for the states. Then, we varied the number of states and obtained the corresponding total angular distribution (the sum of cross sections for all states). We observed that different sets of states provide quite similar (total) cross sections, when their values of deformation parameters and excitation energies are related by the following expressions:

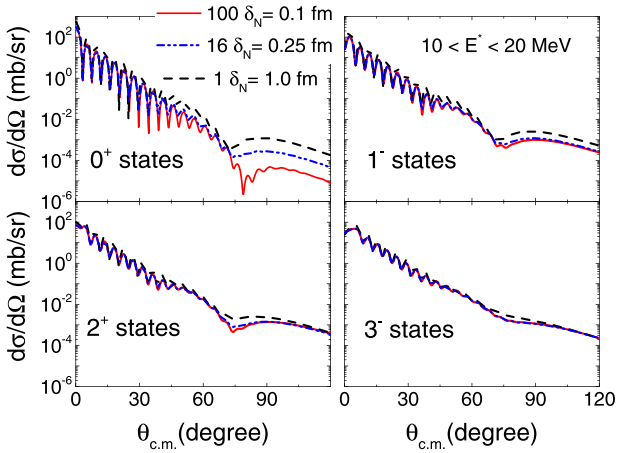

Figure 3. Total (sum over all states) angular distributions obtained for different spins, considering three sets of discrete states in the range $10 \leqslant E^* \leqslant 20$ MeV.

$$\sum_{i=1}^{N_1} \delta_i^2 = \sum_{j=1}^{N_2} \delta_j^2, \tag{73}$$

$$\sum_{i=1}^{N_1} E_i^* \delta_i^2 = \sum_{j=1}^{N_2} E_j^* \delta_j^2, \tag{74}$$

where N_1 and N_2 are the numbers of states of both sets. Figure 3 illustrates this characteristic, presenting results obtained for different spins, and considering three sets of values for $\delta_{\rm N}$ and E^*: i) one hundred states with $\delta_{\rm N} = 0.1$ fm, spaced in regular steps of 0.1 MeV; ii) 16 states with $\delta_{\rm N} = 0.25$ fm in steps of 0.625 MeV; and iii) only one state with $\delta_{\rm N} = 1$ fm at $E^* = 15$ MeV. For all spins, the cross sections obtained with the three different sets are very similar at the forward angular region. Significant differences are observed in the backward region, being these differences smaller for larger spins. Except in the case of 0^+ states, the use of only one state at $E^* = 15$ MeV can simulate quite well a uniform continuous in the region $10 \leqslant E^* \leqslant 20$ MeV.

The density of states necessary to simulate the continuum depends on the region of excitation energy considered. This is illustrated in figure 4, where panels (a) and (b) correspond to spin 0^+ and panels (c) and (d) to spin 2^+. For the 0^+ spin, just one state provides already the same result as 100 states in the region $20 \leqslant E^* \leqslant 30$ MeV (see figure 4(a)). This is in contrast with the behavior at the region of $10 \leqslant E^* \leqslant 20$ MeV (figure 3), where not even 16 0^+ states are enough to simulate the results of 100 0^+ states. Thus, the density of states (necessary to simulate the continuum) is smaller for higher regions of E^*. Of course, the density also depends on the range of the excitation energy region. For instance, 16 states are necessary to reproduce the same cross sections of 100 states in the case of 0^+ at $20 \leqslant E^* \leqslant 80$ (see figure 4(b)). Similar results are obtained for other spin values (see figures 4(c) and (d)).

Reference [19] provides data for the double differential cross sections $\mathrm{d}^2\sigma/\mathrm{d}\Omega\mathrm{d}E^*$, relative to the CPB at the region of excitation energies underneath the observed giant resonances (from $E^* = 10$ to about 15 MeV). Since, as already commented, the cross section

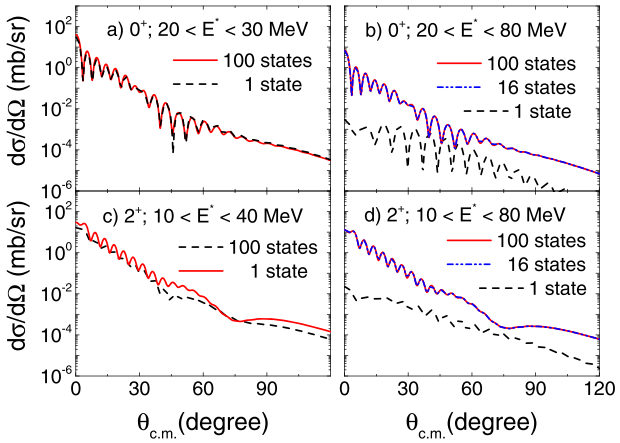

Figure 4. The same as figure 3, for other regions of excitation energies.

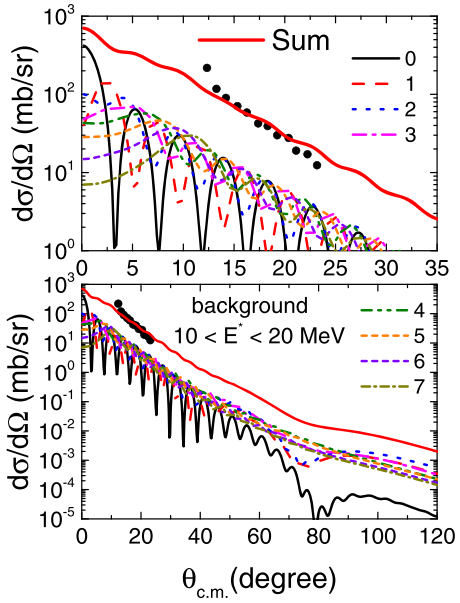

Figure 5. Data and theoretical cross sections for the CPB at the region of excitation energy $10 \leqslant E^* \leqslant 20$ MeV.

decreases very slowly with the excitation energy, we consider that the same double differential cross sections are also valid for $10 \leqslant E^* \leqslant 20$ MeV. The corresponding angular distribution for the CPB was thus obtained by: $\mathrm{d}\sigma/\mathrm{d}\Omega = \Delta E^* \times \mathrm{d}^2\sigma/\mathrm{d}\Omega\mathrm{d}E^*$ with $\Delta E^* = 10$ MeV, and is presented in figure 5. No structure is observed in this experimental angular distribution. Thus, we have simulated the CPB by the sum of cross sections for inelastic states with spins varying from 0 to 7. We have assumed only one state for each spin (with $E^* = 15$ MeV) and the same δ_{N} value for all states. The fit to the data resulted in $\delta_{\mathrm{N}} = 1.2$ fm.

Table 2. The table presents information related to the couplings corresponding to the continuum, as a function of bins of excitation energy. The $\delta_N^{(1)}$ values represent the deformation parameters that result in a total cross section of 25 mb in each bin, when considering only one state for each spin. The $N^{(0.1)}$ values represent the number of states with $\delta_N = 0.1$ fm, for each spin and within each bin, that provides the same total inelastic cross section of 25 mb/bin. $\delta_N^{(2)}$ are the deformation values assumed in the CC calculations when considering only one state for each bin and spin. N_2, $\delta_N^{(3)}$ and ΔE^* are the number of states, the deformation value and the step of excitation energy assumed in other CC calculations (see text for details).

E^*(MeV)	$\delta_N^{(1)}$ (fm)	$N^{(0.1)}$	$\delta_N^{(2)}$ (fm)	N_2	$\delta_N^{(3)}$ (fm)	ΔE^*(MeV)
10 to 20	0.81	66	0.81	16	0.202	0.625
20 to 30	1.17	137	1.17	30	0.213	0.333
30 to 40	2.21	488	2.21	100	0.221	0.1
40 to 50	6.38	4.1×10^3	6.38	150	0.521	0.0667
50 to 60	28.1	7.9×10^4	12	36	2	0.278
60 to 70	98.6	9.7×10^5	12	36	2	0.278
70 to 80	217	4.7×10^6	12	36	2	0.278

Figure 5 presents the cross sections for each state and also the corresponding sum. Considering that we deal only with a simulation, the agreement between data and theoretical results is satisfactory.

The sum of the (angle integrated) cross sections for the discrete inelastic states of table 1 corresponds to about 27 mb. This value is quite realistic and is related to a region of low excitation energies: $2.6 \leqslant E^* \leqslant 13.9$ MeV, whose range is about 11 MeV. In contrast, the CPB discussed above in the region $10 \leqslant E^* \leqslant 20$ MeV results in an angle integrated cross section of 57 mb. This value is more than double that for the discrete states. Thus, probably part of this CPB does not arise from peripheral reaction channels. Besides the instrumental background, the CPB can also include the contribution of particles that come from the compound nucleus evaporation associated to the fusion process.

Taking into account all these results, we consider that the effect of the physical continuum on the elastic channel can be roughly simulated by assuming bins of 10 MeV, from $E^* = 10$ MeV to 80 MeV. In each bin, we included only one state for each spin, ranging from 0 to 7, with the same nuclear deformation value for these 8 states (we assumed $\delta_C = 0$ for the background). The excitation energies for these states are adopted according to the mean value of the corresponding bin. The δ_N value for each bin was adjusted to provide a corresponding total integrated cross section of 25 mb. Table 2 lists the $\delta_N^{(1)}$ values obtained with this procedure as a function of the corresponding bins.

Very large $\delta_N^{(1)}$ values were obtained for high excitation energies. As discussed above and according to expressions (73) and (74), we could obtain the same cross sections by exchanging each single state with this large δ_N value by a number N of states with smaller deformation values as, for instance, $\delta_N = 0.1$ fm. These $N^{(0.1)}$ values are included in table 2 and are presented in figure 6 as a function of the excitation energy. The number of states increases exponentially with the excitation energy. This behavior is already expected since it is well known that the energy levels of heavy nuclei have similar exponential behavior [21].

4.2. The effect of the couplings on the elastic channel

We turn now to the elastic scattering angular distribution at $E_{lab.} = 139$ MeV, measured in a wide angular range, that is presented in logarithmic (a) and linear (b) scales in figure 7. As

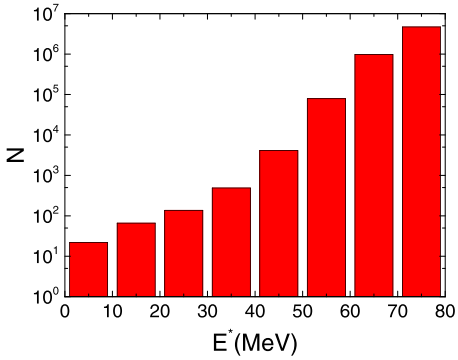

Figure 6. Number of states with $\delta_{\rm N} = 0.1$ fm (for each spin and each bin), that results in a continuum cross section of 25 mb/bin, as a function of the excitation energy.

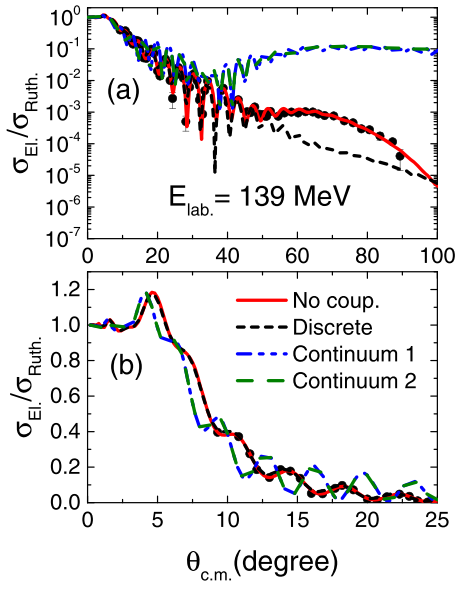

Figure 7. Experimental and theoretical elastic scattering angular distributions in (a) logarithmic and (b) linear scales. The lines correspond to single-channel OM cross sections and to CC results considering: i) only the discrete states of table 1; and ii) the couplings of these states plus those to the continuum, considering two different sets of states to represent the continuum.

already mentioned, the theoretical single-channel OM cross sections (solid red lines in the figure) describe quite well the data. We assume the same OP in the CC calculations in order to evaluate the effect of the inelastic couplings on the elastic scattering cross sections. The short-dashed black lines in figure 7 represent the results of CC calculations, in which only the 22 discrete states of table 1 were coupled. The effect of these couplings on the elastic is negligible at forward angles but it is quite significant at the backward region, particularly in the region of the nuclear rainbow. This result, obtained with realistic calculations with this particular

set of states, already demonstrates the importance of the inelastic couplings for the elastic channel.

We tried to include the couplings to the continuum in the CC calculations, assuming one state for each bin and spin, with deformation values according to $\delta_N^{(1)}$ of table 2. Nevertheless, we could not obtain a satisfactory numerical convergence in this case. In order to overcome this problem, we had to decrease the deformations related to the three last bins, according to the $\delta_N^{(2)}$ values of table 2. The dash-dotted blue lines (continuum 1) in figure 7 represent the calculations including couplings to the continuum and also to the discrete states of table 1. Now, the effect on the cross sections is much larger, affecting also the forward angular region.

With the purpose of testing a possible effect of the variation of the density of states, we have performed another CC calculation with a different set of states for the continuum. N_2, $\delta_N^{(3)}$ and ΔE^* of table 2 are the number of states, the deformation value and the step of spacing for the excitation energy values, in each bin and for each spin, assumed in this CC calculation. According to expressions (73) and (74), this second set of states for the continuum would be equivalent to the first one. Also the 22 discrete states of table 1 were included in these calculations. We emphasise that, in this case, we have considered a total of 3254 excited states with different spins, that resulted in 14 632 CE for each partial wave. The calculation took a computing time of about 9 h. The corresponding results are included as dashed green lines (continuum 2) in figure 7. The two different sets of states adopted for the continuum in fact provide almost identical theoretical cross sections.

Since the OP assumed in our calculations already provides a good description of the data in the context of the OM, the theoretical CC results are in disagreement with the experimental angular distribution. In order to improve the data description within the CC approach, we should readjust the OP parameters to fit the data. This would demand a long time, taking into account that the OP has six free parameters and the search would involve many interactions embracing CC calculations with a large number of couplings. Since the coupling potentials are related to the derivative of the real part of the OP, also the deformation parameters would be adjustable parameters involving as well the fit to the experimental inelastic cross sections in addition to the elastic ones. This study is beyond the scope of the present work.

Moreover, with the present CC calculations we have already obtained the polarization potential associated to the inelastic couplings. Therefore, we can compare the polarization with the OP used in our calculations. In figure 8, we show the real (panels a and b) and imaginary (panels c and d) parts of the OP as solid black lines, and also the MPP (dotted red lines) and the TLEP (dash-dotted blue lines) for the grazing angular momentum ($J = 48$) for $E_{\text{lab.}} = 139$ MeV. These polarization potentials were obtained in the case of couplings only to the discrete states of table 1. Panels (b) and (d) present the potentials in a wider scale at the region of the s-wave barrier radius. Clearly, the polarization strengths are comparable with those for the OP. Therefore, if we were to readjust the OP to fit the data in the CC approach, the resulting OP probably would be quite different of that obtained within the OM context.

4.3. Comparison between results of the traditional and new methods

To the best of our knowledge, heretofore the solution of CE involving thousands of states could not be performed in practice. Even coupled discretised continuum channel calculations typically involve tens or a few hundred states (see e.g. references [22, 23]), considering excitation energies that usually reach about 10 MeV. As already mentioned, with the new

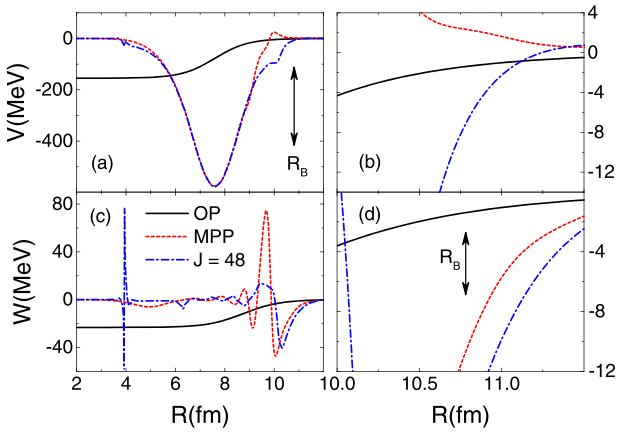

Figure 8. Real (panels a and b) and imaginary (panels c and d) parts of the optical potential (OP), MPP and TLEP in the case of couplings only to the discrete excited states. The arrows in the figure represent the approximate position of the s-wave barrier radius.

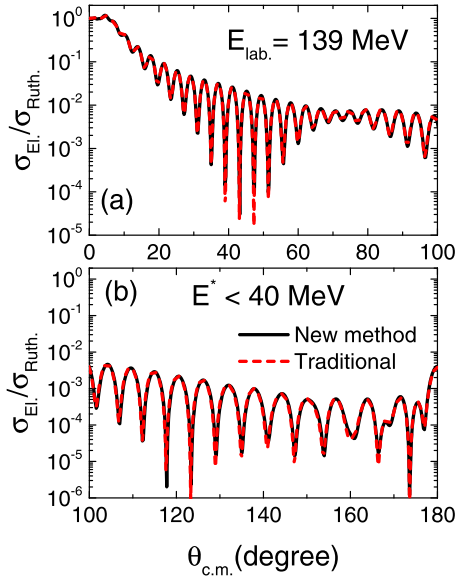

Figure 9. Theoretical CC elastic scattering angular distributions obtained with the new and traditional methods for solving CE, considering states that also include the bin corresponding to $30 \leqslant E^* \leqslant 40$ MeV. The forward and backward angular regions are shown in panels (a) and (b), respectively.

method we have solved CE involving 3254 excited states with excitation energies that reach 80 MeV.

In order to compare and check the results, in many cases we have performed calculations with the new method for solving the CE and with the usual methods of appendix A. In this section, we illustrate the results obtained in a small part of our tests with some examples.

In these cases, we used the FRESCO code to solve the CE through the traditional method described in appendix A. However, within the coupling model presented in section 3, our version of the FRESCO code is prepared only for couplings to inelastic states with spins in the region of $1 \leqslant S \leqslant 6$. Thus, in the cases of the CC results presented in this sub-section, we do not include states with $S = 0$ and $S = 7$.

We performed CC calculations at $E_{\text{lab.}} = 139$ MeV, with $R_{\text{Max}} = 20$ fm, step size $\Delta r = 0.02$ fm and angular momenta up to $J_{\text{Max}} = 100$ (grazing corresponds to $J = 48$). In addition to the set of discrete states of table 1, in these calculations we included, one at a time, the lowest bins of table 2, with nuclear deformations given by $\delta_{\text{N}}^{(2)}$ (for $S = 1$ to 6). The theoretical elastic scattering cross sections obtained with the traditional and new methods are identical in all tests performed, until including the third bin ($30 \leqslant E^* \leqslant 40$ MeV). The theoretical cross sections (with the inclusion of the third bin) obtained with both methods are shown in figures 9(a) and (b), in the forward and backward angular regions, respectively.

When we included more than 3 bins of table 2 in the CC calculations, the numerical results of the traditional method obtained with the FRESCO code no longer converged. In this case, we also tried the iterative method (with FRESCO) without success.

The FRESCO code can also be used within the context of the *R*-matrix calculations. As mentioned in appendix A.3, the usual *R*-matrix method and the new one are equivalent in terms of stability of the numerical convergence. On the one hand, the usual *R*-matrix method has no limitation concerning the coupling model. On the other hand, our method has only adjustable parameters related to the elastic wave-function, the a_n values of equation (31), while the usual *R*-matrix has a bidimensional spectrum of parameters related to all channels (the a_{in} of equation (A.3)). The larger number of parameters can become a problem when dealing with many CE, due to the amount of memory and computing time required to perform the calculations. Indeed, using FRESCO with this option we obtained convergent results only in the case of couplings to the 21 discrete states of table 1, with a computing time of about 15 h. We tried to include more states but the time became prohibitive. The new method did the same job with the 21 states in only 2.4 min.

5. Conclusion

We have presented a new method to solve CE that is faster and involves a less degree of problems with numerical convergence in relation to other usual methods. However, the new technique can be used only in the case of direct couplings of the inelastic states to the elastic channel.

With this new method, we analyzed a wide data set containing experimental elastic and inelastic scattering angular distributions for ^{4}He + ^{208}Pb at energies about 35 MeV/nucleon. We obtained realistic values for the deformation parameters of 22 ^{208}Pb discrete excited states through DWBA calculations. We have also included a continuum of inelastic states in our analyses within a quite schematic calculation. Different of the case of the discrete states, the results concerning to the continuum should be considered just as a rough estimate of its effect.

We have demonstrated that the effect of the inelastic couplings on the theoretical elastic scattering cross sections is quite significant, even in the case where only the discrete states were explicitly coupled. The corresponding polarization potential has strengths comparable to those of the OP. Therefore, at least part of the energy dependence observed for phenomenological OP that describe experimental elastic scattering angular distributions within OM should be related to couplings with states of high excitation energies. The effects of these inelastic couplings should also be quite important at low energies, near the Coulomb barrier, as we have demonstrated in earlier works [11, 24].

There is room to expand studies on this topic, both from theoretical and experimental points of view. Indeed, the continuum should be subject of new experiments, in order to measure the charge and mass in addition to the energy of the particles, with the purpose of identification of those events that actually arise from peripheral reactions.

Acknowledgments

L C Chamon thanks Prof. Pierre Descouvemont for useful discussions about the R-matrix method. This work was partially supported by Fundação de Amparo à Pesquisa do Estado de São Paulo (FAPESP, Brazil) Proc. Nos. 2018/04965-4, 2018/09998-8, 2019/07767-1 and 2019/05769-7; by Conselho Nacional de Desenvolvimento Científico e Tecnológico (CNPq, Brazil) Proc. Nos. 302160/2018-3 and 304056/2019-7; and by project INCT-FNA Proc. No. 464898/2014-5.

Appendix A. Usual methods to solve coupled equations

In this appendix, we describe briefly three usual methods do solve CE. The description is adapted for the problem raised in the beginning of section 2.

A.1. The traditional method

The set of CE (1) and (2) can be integrated from $r = 0$ to $r = R_{\text{Max}}$ using the Numerov method [16]. Within this method, the r space is discretised in r_j values, similarly to what we do in our own method. If one knows the wave-function values for the first r_1, the numerical integration can be performed progressively towards $r = R_{\text{Max}}$ in steps Δr. However, we do not know the values of the wave-functions at r_1 *a priori*.

In order to overcome this problem, we use the linearity of the set of CE. Using the Numerov method, we solve the CE by integration $M + 1$ times. In each time, we use a different set of wave-functions values at r_1. For instance, all wave-functions are zero out, except one, for which we set the value 1. This process is repeated progressively $M + 1$ times, resulting in a set of $M + 1$ solutions (each solution is a set of wave-functions) linearly independent. Then, we perform a linear combination with these $M + 1$ solutions, in order to obtain a behavior at $r = R_{\text{Max}}$ according to the boundary conditions (5) and (6). With this, we solve the CC problem.

Note that the traditional method implies in solving $M + 1$ times a set of $M + 1$ CE. Thus, the time of computation is nearly proportional to M^2, becoming prohibitive for large M values (many coupled states).

Due to numerical problems like, for instance, truncation, not always the resulting computational solution is in fact a true solution of the CC problem. A possible form the check the convergence of the results is varying the R_{Max} and Δr values. Another form to check the numerical results is testing the flux conservation (as we have done in our method). Finally, there is even other form to check the results. Having the final solution, one knows the values of all wave-functions at r_1. Then, one can input these values and run again the Numerov method up to R_{Max}. This second solution of the CC problem should be equal to the first one, at least in the region of large r values where the S matrix is obtained.

A.2. The iterative method

The iterative method involves the solution of equations (13) and (14) to find the wave-functions and, with them, to obtain the S matrix with equations (15) and (16). According to its name, the

method uses an iterative procedure, which is based on the following equations:

$$f_0^{(n+1)}(r) = f_0^{\rm op}(r) - \frac{k_0}{E}\left\{ f_0^{\rm op}(r)\int_r^\infty f_0^{\rm irr}(r')\sum_{i=1}^{M}\left[V_i(r')\,f_i^{(n)}(r')\right]{\rm d}r' + f_0^{\rm irr}(r)\int_0^r f_0^{\rm op}(r')\sum_{i=1}^{M}\left[V_i(r')\,f_i^{(n)}(r')\right]{\rm d}r'\right\}, \tag{A.1}$$

$$f_i^{(n+1)}(r) = -\frac{k_0^2}{k_i E}\left[f_i^{\rm op}(r)\int_r^\infty f_i^{\rm irr}(r')V_i^*(r')\,f_0^{(n)}(r'){\rm d}r' + f_i^{\rm irr}(r)\int_0^r f_i^{\rm op}(r')V_i^*(r')\,f_0^{(n)}(r'){\rm d}r'\right]. \tag{A.2}$$

These equations are very similar to (13) and (14), except by the wave-functions which are now labeled as $f_i^{(n)}$ or $f_i^{(n+1)}$ instead of f_i.

In the first iteration, $n = 0$, we assume $f_0^{(0)}(r) = f_0^{\rm op}(r)$ and $f_i^{(0)}(r) = 0$. With this in equations (A.1) and (A.2), we obtain $f_0^{(1)}(r)$ and $f_i^{(1)}(r)$. Observe that, at this stage, the elastic wave-function is still equal to the optical one, $f_0^{(1)}(r) = f_0^{\rm op}(r)$, but the inelastic wave-functions are not vanishing anymore. If we stop the method at this stage, the respective solutions are named as the DWBA.

We can proceed with the iterations, increasing the n values up to a certain point, in which we obtain: $f_i^{(n+1)}(r) = f_i^{(n)}(r)$ (within a required precision) for all states. If we obtain this, then the CC problem is solved exactly. Alternatively, we may require that $S_i^{(n+1)} = S_i^{(n)}$ (again within a certain precision) to stop the iterations. There is no guarantee that the method will converge and, in certain cases, it does not.

A.3. The R-matrix method

We recommend reference [6] for a detailed description of the R-matrix method. The method is based on an expansion of the elastic and inelastic wave-functions:

$$f_i(r) \approx \sum_{n=1}^{N} a_{\rm in}\,\phi_n(r). \tag{A.3}$$

With this, one search for the $a_{\rm in}$ coefficient values with a procedure similar to that applied in our new method. The R-matrix method provides good numerical convergence (depending on the number of base functions adopted). An advantage of this method in relation to the new one of this work is that the R-matrix method can be used for any coupling model (our method has a limitation for the coupling model, as already discussed). On the other hand, the R-matrix method requires the use of bidimensional parameters, $a_{\rm in}$, since it expands not only the elastic wave-function (as in our method), but also the wave functions for all other states. Thus, when the number of states is very large, the R-matrix method deals with the inversion of a huge matrix, that can result, again, in difficult numerical problems or also in extremely long computing time.

ORCID iDs

L C Chamon https://orcid.org/0000-0001-9624-0882

References

[1] Satchler G R 1983 *Direct Nuclear Reactions* (Oxford: Clarendon)
[2] Thompson I J and Nunes F M 2009 *Nuclear Reactions for Astrophysics: Principles, Calculations and Applications of Low-Energy Reactions* (Cambridge: Cambridge University Press)
[3] Raynal J 1986 1986 Coupled Channel Formalism and ECIS Code *Meeting on the Use of the Optical Model for the Calculation of Neutron Cross Sections Below 20 MeV* (OECD/NEA)
[4] Raynal J 1981 *Phys. Rev.* C **23** 2571
[5] Thompson I J 1988 *Comput. Phys. Rep.* **7** 167
[6] Descouvemont P 2016 *Comput. Phys. Commun.* **200** 199 and references therein
[7] Brandan M E and Satchler G R 1997 *Phys. Rep.* **285** 143
[8] Kobos A M, Brown B A, Hodgson P E, Satchler G R and Budzanowski A 1982 *Nucl. Phys.* A **384** 65
[9] Hussein M S, Rego R A and Bertulani C A 1991 *Phys. Rep.* **201** 279
[10] Chamon L C *et al* 2002 *Phys. Rev.* C **66** 014610
[11] Chamon L C and Gasques L R 2016 *J. Phys. G: Nucl. Part. Phys.* **43** 015107
[12] Cowell P H and Gormmelin A C D 1910 *Investigation of the Motion of Halley's Comet: Appendix to Greenwich Observations for 1909* (Edinburgh, UK: Greenwich Royal Observatory) p 84
[13] Manning M F and Millman J 1939 *Phys. Rev.* **53** 673
[14] Helene O 2006 *Método dos Mínimos Quadrados com Formalismo Matricial* (São Paulo, Brazil: Editora Livraria da Fisica)
[15] Satchler G R, Nagarajan M A, Lilley J S and Thompson I J 1987 *Ann. Phys., NY* **178** 110
[16] Raynal J 1972 Optical-model and coupled-channel calculations in nuclear physics *Computing as a Language of Physics* (Vienna: IAEA) p 281
[17] Thompson I J, Nagarajan M A, Lilley J S and Smithson M J 1989 *Nucl. Phys.* A **505** 84
[18] Goldberg D A, Smith S M, Pugh H G, Roos P G and Wall N S 1973 *Phys. Rev.* C **7** 1938
[19] Harakeh M N, Van Heyst B, Van Der Borg K and Van Der Woude A 1979 *Nucl. Phys.* A **327** 373
[20] Dennert H *et al* 1995 *Phys. Rev.* C **52** 3195
[21] von Egidy T and Bucurescu D 2005 *Phys. Rev.* C **72** 044311
[22] Diaz-Torres A and Thompson I J 2002 *Phys. Rev.* C **65** 024606
[23] Diaz-Torres A, Thompson I J and Beck C 2003 *Phys. Rev.* C **68** 044607
[24] Chamon L C, Gasques L R, Nobre G P A, Rossi E S Jr, deBoer R J, Seymour C, Wiescher M and Kiss G G 2015 *J. Phys. G: Nucl. Part. Phys.* **42** 055102